The Astrophysical Journal Letters, 957:L22 (14pp), 2023 November 10 https://doi.org/10.3847/2041-8213/acf5ec

JWST Reveals Excess Cool Water near the Snow Line in Compact Disks, Consistent with Pebble Drift

Andrea Banzatti[1], Klaus M. Pontoppidan[2], John S. Carr[3], Evan Jellison[1], Ilaria Pascucci[4], Joan R. Najita[5], Carlos E. Muñoz-Romero[7], Karin I. Öberg[6], Anusha Kalyaan[1], Paola Pinilla[7], Sebastiaan Krijt[8], Feng Long[9,18], Michiel Lambrechts[10], Giovanni Rosotti[11], Gregory J. Herczeg[12], Colette Salyk[13], Ke Zhang[14], Edwin A. Bergin[15], Nicholas P. Ballering[16], Michael R. Meyer[15], and Simon Bruderer[17]
The JDISCS Collaboration
[1] Department of Physics, Texas State University, 749 North Comanche Street, San Marcos, TX 78666, USA; banzatti@txstate.edu
[2] Jet Propulsion Laboratory, California Institute of Technology, 4800 Oak Grove Drive, Pasadena, CA 91109, USA
[3] Department of Astronomy, University of Maryland, College Park, MD 20742, USA
[4] Department of Planetary Sciences, University of Arizona, 1629 East University Boulevard, Tucson, AZ 85721, USA
[5] NSF's NOIRLab, 950 North Cherry Avenue, Tucson, AZ 85719, USA
[6] Center for Astrophysics, Harvard & Smithsonian, 60 Garden Street, Cambridge, MA 02138, USA
[7] Mullard Space Science Laboratory, University College London, Holmbury St Mary, Dorking, Surrey RH5 6NT, UK
[8] School of Physics and Astronomy, University of Exeter, Stocker Road, Exeter EX4 4QL, UK
[9] Lunar and Planetary Laboratory, University of Arizona, Tucson, AZ 85721, USA
[10] Center for Star and Planet Formation, GLOBE Institute, University of Copenhagen, Øster Voldgade 5-7, DK-1350 Copenhagen, Denmark
[11] Dipartimento di Fisica, Universitá degli Studi di Milano, via Giovanni Celoria 16, I-20133, Milano, Italy
[12] Kavli Institute for Astronomy and Astrophysics, Peking University, Beijing 100871, People's Republic of China
[13] Department of Physics and Astronomy, Vassar College, 124 Raymond Avenue, Poughkeepsie, NY 12604, USA
[14] Department of Astronomy, University of Wisconsin–Madison, Madison, WI 53706, USA
[15] Department of Astronomy, University of Michigan, 1085 South University Avenue, Ann Arbor, MI 48109, USA
[16] Department of Astronomy, University of Virginia, Charlottesville, VA 22904, USA
[17] Max-Planck-Institut für extraterrestrische Physik, Gießenbachstraße 1, D-85748 Garching bei München, Germany
Received 2023 July 7; revised 2023 August 25; accepted 2023 August 30; published 2023 November 8

Abstract

Previous analyses of mid-infrared water spectra from young protoplanetary disks observed with the Spitzer-IRS found an anticorrelation between water luminosity and the millimeter dust disk radius observed with ALMA. This trend was suggested to be evidence for a fundamental process of inner disk water enrichment proposed decades ago to explain some properties of the solar system, in which icy pebbles drift inward from the outer disk and sublimate after crossing the snow line. Previous analyses of IRS water spectra, however, were uncertain due to the low spectral resolution that blended lines together. We present new JWST-MIRI spectra of four disks, two compact and two large with multiple radial gaps, selected to test the scenario that water vapor inside the snow line is regulated by pebble drift. The higher spectral resolving power of MIRI-MRS now yields water spectra that separate individual lines, tracing upper level energies from 900 to 10,000 K. These spectra clearly reveal excess emission in the low-energy lines in compact disks compared to large disks, demonstrating an enhanced cool component with $T \approx 170$–400 K and equivalent emitting radius $R_{eq} \approx 1$–10 au. We interpret the cool water emission as ice sublimation and vapor diffusion near the snow line, suggesting that there is indeed a higher inward mass flux of icy pebbles in compact disks. Observation of this process opens up multiple exciting prospects to study planet formation chemistry in inner disks with JWST.

Unified Astronomy Thesaurus concepts: Protoplanetary disks (1300); Exoplanet formation (492); Molecular spectroscopy (2095); Young stellar objects (1834); Classical T Tauri stars (252); Infrared spectroscopy (2285); Circumstellar disks (235); Planet formation (1241); Star formation (1569); Pre-main sequence stars (1290)

1. Introduction

The dynamics and accretion of pebbles[19] in disks are currently proposed to be fundamental for forming planets within protoplanetary disk lifetimes (e.g., Lambrechts & Johansen 2012; Levison et al. 2015) and determining both the mass architecture and chemical composition of planetary systems (e.g., Ida et al. 2016; Bitsch et al. 2019a, 2019b; Cridland et al. 2019; Lambrechts et al. 2019). High-resolution continuum imaging with the Atacama Large Millimeter/submillimeter Array (ALMA) shows that protoplanetary disks with ages of a few megayears can have a wide range of sizes (10–200 au), where systems of rings and gaps are frequently observed in large disks (e.g., Andrews 2020; Bae et al. 2022, for recent reviews). It has been suggested that the wide range in disk sizes may be due to hydrodynamical processes where large disks retain pebbles in systems of rings (Pinilla et al. 2012), while compact disks have shrunk under the effect of efficient inward "pebble drift" delivering solids to the inner planet-forming region (e.g., Rosotti et al. 2019; Appelgren et al. 2020; Zormpas et al. 2022). Such pebble drift should have fundamental implications for inner disk chemistry; icy pebbles that migrate inward from the outer disk will sublimate after crossing the snow line, producing a time-dependent water

[18] NASA Hubble Fellowship Program Sagan Fellow.
[19] Solid particles with diameters between a millimeter and a meter.

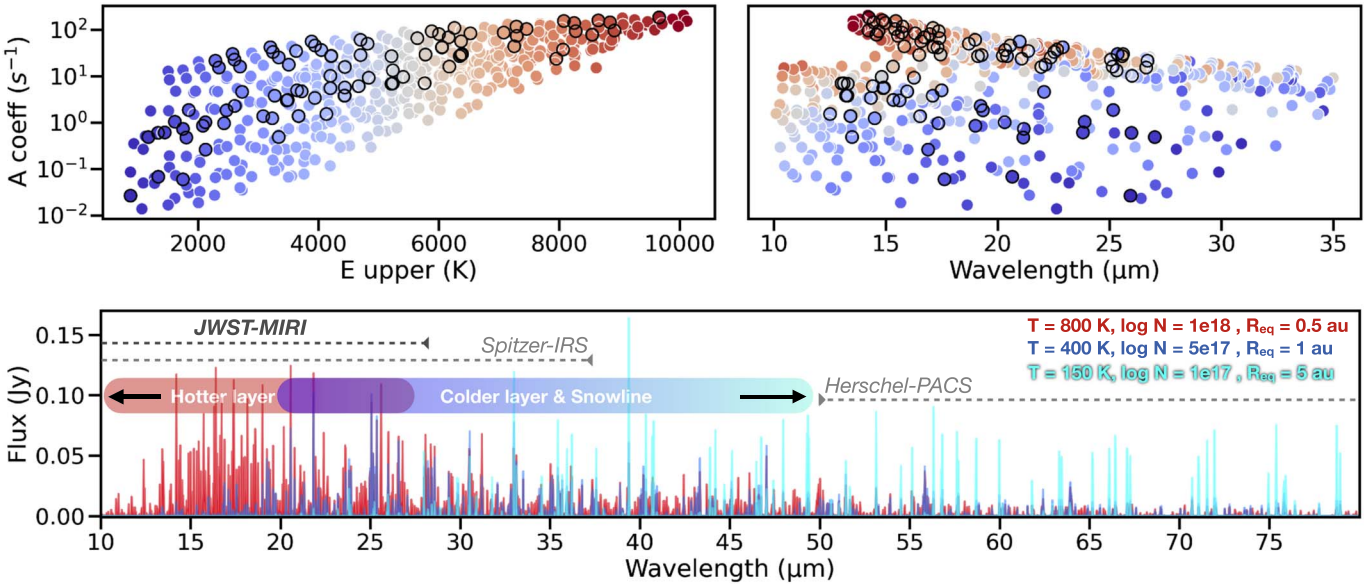

Figure 1. The distribution of upper level energies E_u and Einstein-A coefficients (top panels, with color-coding reflecting E_u values) across infrared wavelengths naturally traces radial temperature gradients in inner disks within and across the water snow line (bottom panel, where the spectrum is scaled to a distance of 130 pc). This figure is partly adapted from Figure 1 in Blevins et al. (2016) and Figure 13 in Banzatti et al. (2023). The MIRI lines used in the analysis in Section 3 are marked with black circles.

abundance. This systemic process was proposed to explain radial chemical gradients measured in meteorites, the formation of Jupiter's core, and water depletion in rocky planets in the inner solar nebula (Morfill & Voelk 1984; Stevenson & Lunine 1988; Cyr et al. 1998; Ciesla & Cuzzi 2006; Morbidelli et al. 2016). More recently, this process was modeled by Kalyaan et al. (2021) in the context of disk structures observed with ALMA, finding that the inner disk water enrichment could indeed be regulated by the presence (or absence) of gaps that retain icy pebbles in the outer disk and prevent them from entering the region of the snow line.

That inner disks (a region within a few au from the central star) may host large columns of warm water vapor was first revealed from mid-infrared medium-resolution spectroscopy (Carr & Najita 2008; Salyk et al. 2008) observed from space with the Spitzer-IRS (Houck et al. 2004). A dense forest of water emission lines, in addition to transitions and bands from OH, HCN, C_2H_2, and CO_2, were identified, tracing molecular budgets and chemistry in the terrestrial planet-forming region of class II disks (e.g., review by Pontoppidan et al. 2014). Over the past 15 yr, analyses of ≈100 disk spectra observed with Spitzer revealed the general properties and some trends of the inner molecular reservoir, including heating by stellar and accretion irradiation, depletion of molecules in disks with large inner dust cavities, and chemical differences as a function of stellar mass and luminosity (e.g., Pontoppidan et al. 2010a; Carr & Najita 2011; Salyk et al. 2011b; Pascucci et al. 2013; Walsh et al. 2015; Banzatti et al. 2017; Woitke et al. 2018). A particularly remarkable trend linking very different disk regions was recently found from the combined analysis of Spitzer spectra and ALMA continuum imaging. Expanding on earlier results from Najita et al. (2013), Banzatti et al. (2020) reported an anticorrelation between the infrared water line luminosity tracing gas within a few au and the distribution of solid pebbles at 10–200 au in disks. That is, radially compact disks show a stronger water line luminosity than large disks. This correlation was tentatively interpreted in the context of pebble drift. The proposed mechanism is that pebble drift through the water snow line will enrich the inner disk oxygen abundance and, in turn, the oxygen/carbon (O/C) ratio (e.g., Bosman et al. 2017; Booth & Ilee 2019; Cevallos Soto et al. 2022). A higher O/C ratio will, in turn, produce a higher water abundance that may be observed as a stronger water line luminosity, according to disk chemical models (e.g., Najita et al. 2011; Woitke et al. 2018; Anderson et al. 2021).

However, previous analyses were limited by the relatively low spectral resolving power of Spitzer-IRS ($R \approx 700$, or 450 km s^{-1}). Because of severe line blending, detailed physical properties of the emitting gas could not be retrieved to high levels of confidence. This was particularly true for water, where line blending across the forest of ≈1000 emission lines led to uncertainties in column densities and abundances of 1–3 orders of magnitude (e.g., Carr & Najita 2011; Salyk et al. 2011a; Banzatti 2013; James et al. 2022). While high-resolution ($R \sim 10{,}000$–$100{,}000$) spectroscopy from the ground can resolve individual water lines, these are limited by telluric transmission to narrow ranges of higher-excitation lines probing only an inner, optically thick, hotter region (500–1200 K; Pontoppidan et al. 2010b; Najita et al. 2018; Salyk et al. 2019; Banzatti et al. 2023). A precise analysis of water spectra across infrared wavelengths remains a challenge today due to the complex combination of radial and vertical gradients in temperature and density, which can produce non-LTE excitation in some disk regions, and the need to observe large spectral ranges at high resolving power (e.g., Meijerink et al. 2009; Bosman et al. 2022; Banzatti et al. 2023).

Mitigating these challenges, the asymmetric top geometry of the water molecule leads to a very large number of rotational transitions that naturally trace radial temperature gradients, provided a wide spectral range can be observed. Water transitions from a range of upper levels (with energy $E_u \approx 150$–$10{,}000$ K) and Einstein-A coefficients ($A_{ul} \approx 0.01$–100 s^{-1}) extend across the near- to far-infrared wavelength range, where cooler and optically thinner transitions are generally more accessible at longer wavelengths (Figure 1; see also, e.g., Blevins et al. 2016; Notsu et al. 2016). Previous work combining mid- and far-infrared

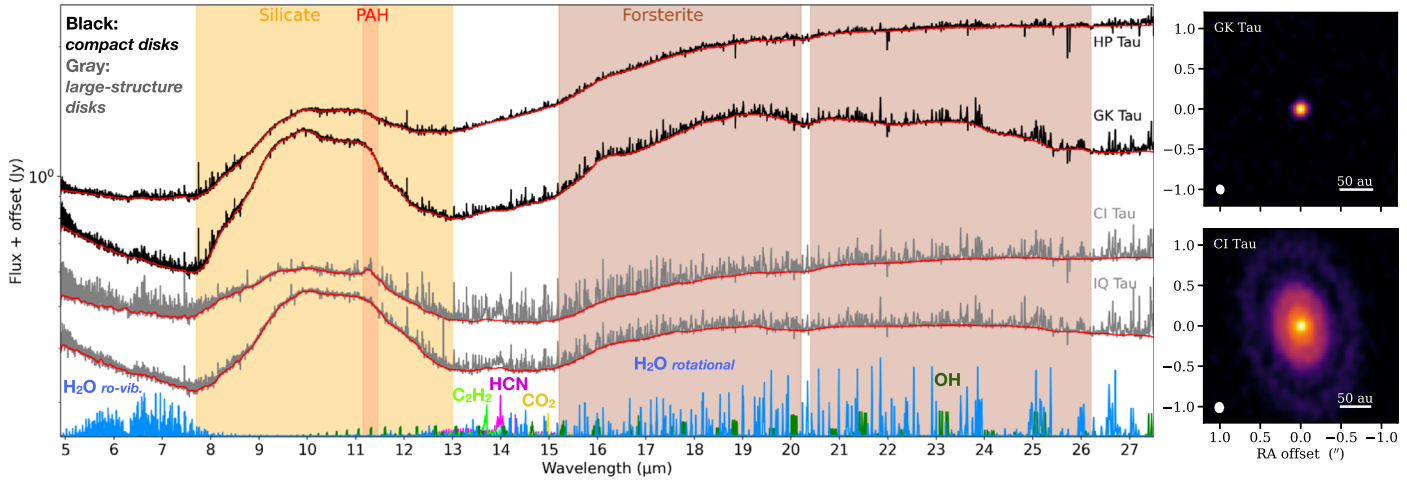

Figure 2. JWST-MIRI-MRS spectra for the four disks. For clarity, the spectra are offset vertically by the following additive shifts: 0.05 Jy in CI Tau, 0.17 Jy in GK Tau, and 0.4 Jy in HP Tau. Illustrative models of molecular emission are shown for guidance at the bottom. Prominent dust features are approximately identified and marked with shaded regions. The estimated continuum that is subtracted before analyzing the water spectra is shown in red on each spectrum. Two ALMA images are shown on the right for reference regarding disk sizes and structures (the whole sample is included in Appendix A).

Table 1
Sample Properties

Name	Dist. (pc)	$T_{\rm eff}$ (K)	$M_\star$ ($M_\odot$)	$L_\star$ ($L_\odot$)	log $L_{\rm acc}$ ($L_\odot$)	log $M_{\rm acc}$ ($M_\odot$ yr^{-1})	n_{13-26}	$R_{\rm disk}$ (au)	Incl. (deg)	CO FW10%–50% (km s^{-1})	$R_{\rm CO}$ 10%–50% (au)	$R_{\rm snow}$ (au)
CI Tau	160	4162	0.65	1.65	−0.7	−7.6	−0.51	190.5	50	265–105	0.02–0.12	2.7
GK Tau	129	4067	0.58	1.48	−1.39	−8.67	−0.40	12.9	39	180–85	0.03–0.11	0.9
HP Tau	177	4375	0.84	1.89	−1.09	−8.17	0.06	22.1	18	115–40	0.02–0.18	1.7
IQ Tau	131	3704	0.42	0.86	−1.40	−8.54	−0.74	109.6	62	190–150	0.03–0.05	0.9

Note. Distances are from Gaia DR3 (Gaia Collaboration et al. 2016, 2022); stellar and accretion properties are from Herczeg & Hillenbrand (2014), Donati et al. (2020), Manara et al. (2023), and Gangi et al. (2022); $R_{\rm disk}$ and disk inclinations are from Long et al. (2019); n_{13-26} is measured from the MIRI spectra in this work; near-infrared CO line widths are measured at 10% and 50% of the line peak from the stacked profiles shown in Appendix A; $R_{\rm CO}$ is the Keplerian radius of infrared CO emission from the half line width velocities at 10% and 50%; and $R_{\rm snow}$ is an expectation for the midplane snow line radius as set by accretion following Equation (2) in Mulders et al. (2015), as previously adopted for a general comparison across disks in Banzatti et al. (2017).

water spectra from Spitzer and Herschel showed that the region near the water snow line at a temperature of ≈150 K dominates the observed water spectrum at ≈25–180 μm (Zhang et al. 2013; Blevins et al. 2016), whereas hotter gas within the snow line dominates the emission at shorter wavelengths (Figure 1). While the wavelength range of the Mid-Infrared Instrument (MIRI) on the James Webb Space Telescope (JWST; Gardner et al. 2023) is therefore most focused on hotter water emission (including the rovibrational bands at <9 μm), cooler water emission with temperatures of ≈150–500 K, just inward of the snow line region, can still be traced at wavelengths as short as ≈20 μm (Zhang et al. 2013; Blevins et al. 2016), well within the MIRI range.

While more complex models that include global temperature gradients (150–1200 K) and non-LTE excitation are currently being explored to fit the entire range of MIRI spectra, in this Letter we investigate the effects of ice sublimation at the snow line in a relative sense by following recent modeling explorations (Kalyaan et al. 2021, 2023) and addressing this question: what is the difference between water spectra in compact disks, which should be enriched in warm water due to efficient pebble drift, versus large disks with gaps, which should be relatively deficient in water due to pebble trapping at larger radii? The analysis of MIRI spectra in this paper finds evidence in support of water enrichment by pebble drift by spectrally separating water lines that were previously blended in Spitzer-IRS spectra and revealing an excess cool water reservoir near the snow line region in compact disks.

2. Sample and Observations

We present MIRI spectra of four protoplanetary disks around single stars in the Taurus star-forming region with ages estimated at 2–3 Myr by Long et al. (2019) using nonmagnetic evolutionary tracks from Feiden (2016). The disks were selected from the sample of Long et al. (2019) to have similar stellar and accretion luminosity to minimize the difference in water spectra due to luminosity effects (Banzatti et al. 2020). The disks were also selected to span a wide range in measured millimeter dust disk sizes to maximize the relative difference in inner disk water abundance expected in the pebble drift scenario (Table 1). Figure 2 and Appendix A show the ALMA images for the four disks with a spatial resolution of 0.″12 from Long et al. (2019). The two large disks, CI Tau and IQ Tau, have multiple resolved gaps and rings at radial locations as small as 10 au and as large as 150 au (Clarke et al. 2018; Long et al. 2018), while the two compact disks are among the smallest known around solar-mass stars (10–20 au). The compact disks are resolved by ALMA but do not show any substructures or millimeter emission at larger disk radii (see more in Section 4). As a measure of the pebble disk radius,

$R_{\rm disk}$, we use the millimeter continuum radius encircling 95% of the total integrated flux density from Long et al. (2019).

We note that HP Tau might have a small inner dust cavity, as suggested by the relatively high infrared index n_{13-26} measured in MIRI spectra instead of the Spitzer-based n_{13-30} index (see Appendix D in Banzatti et al. 2020). The ALMA image with 0.″12 resolution does not resolve this putative cavity, even with superresolution techniques (Jennings et al. 2022b; Zhang et al. 2023), suggesting that the cavity, if present, is smaller than <2 au in width (the smallest dust structure detected with this technique in disks).

The disks were observed over the full wavelength coverage of 4.9–28 μm with the Medium Resolution Spectrometer (MRS; Wells et al. 2015) mode on MIRI (Rieke et al. 2015; Wright et al. 2023) as part of program GO-1640 in Cycle 1. Figure 2 shows the four MIRI-MRS spectra obtained on 2023 February 27–28 with deep integrations (≈1000 s in GK Tau and HP Tau and ≈1800 s in CI Tau and IQ Tau) and reduced as described in Pontoppidan et al. (2023, hereafter Paper I from the JDISCS collaboration). Two standard calibrators (asteroids) from program GO-1549 were used to maximize the quality of fringe removal, the spectral response function, and the flux calibration across the four MIRI channels (Paper I). Target acquisition was used to ensure pointing precision and match across different targets and the asteroids to subpixel levels. An improved wavelength calibration was applied from cross-correlating 200 molecular lines across MIRI wavelengths, improving the precision from ≈90 km s^{-1} down to better than 5 km s^{-1}. The spectra were continuum-subtracted using an iterative median filter with a box of ≈100 pixels and a smoothing step using a second-order Savitzky–Golay filter (Paper I). The MIRI spectra and continua are shown in Figure 2.

As the MIRI resolving power of $R = 1500$–3500 (90–200 km s^{-1}) cannot resolve the gas kinematics (Labiano et al. 2021), in Appendix A, we report for reference the high-resolution ($R \approx 6$–9×10^4, or 3–5 km s^{-1}) line profiles for the CO fundamental band as observed from the ground. Objects CI Tau and GK Tau have comparable CO line profiles, suggesting that their molecular gas radial distribution in the inner disk should be similar. Object IQ Tau shows more compact emission, possibly due to the higher disk inclination (Banzatti et al. 2022), while HP Tau may have a small inner dust cavity (see above). Therefore, while we study all four disks, our analysis below will particularly focus on the comparison between CI Tau (large disk with gaps) and GK Tau (compact disk).

3. Analysis and Results

As summarized in Section 1, cool water emission from the region near the snow line should dominate the emission observed in lower energy levels at longer infrared wavelengths. However, different temperatures contribute different fractions of line flux across a wide range of wavelengths depending on the upper level energy of a specific transition (Figure 1). While single-temperature LTE models have been used to successfully reproduce limited portions of water spectra observed with MIRI (Grant et al. 2023; and Appendix C), modeling the entire MIRI wavelength range should generally be required to include multiple temperature components or a radial temperature gradient (Blevins et al. 2016; Liu et al. 2019; Banzatti et al. 2023; Gasman et al. 2023). Further, non-LTE excitation is likely important for the higher-energy lines with $E_u \gtrsim 4500$ K (Meijerink et al. 2009; Banzatti et al. 2012). Since such modeling is computationally expensive and will suffer from some degree of degeneracy, to address the specific question of this work we employ an empirical method to separate representative temperature components by using the observed water spectra themselves as templates for comparison between small versus large disks as follows.

Spitzer-IRS water spectra from disks have been found to be very similar at 12–16 μm as observed with Spitzer-IRS, suggesting that a different emitting area (i.e., a simple scaling factor that does not change the line ratios in this range) could account for most of the difference in water luminosity between different sources (Salyk et al. 2011b; Carr & Najita 2011). Previous work also found that the dominant correlation with water luminosities (for disks with detected water emission) is with accretion luminosity (Banzatti et al. 2020), consistent with UV irradiation from stellar accretion playing an important role in the heating and excitation of water by driving the size of the emitting area (e.g., Walsh et al. 2015; Najita & Ádámkovics 2017; Woitke et al. 2018; Bosman et al. 2022). Comparisons of water spectra across different disks therefore require normalization of the total water line luminosity to remove the primary effect of a luminosity-dependent emitting area from disk to disk. Indeed, the anticorrelation between water emission and the millimeter dust disk radius was found after normalizing the measured water luminosity with the stellar accretion luminosity (Figure 6 in Banzatti et al. 2020).

To test the correlations previously found with water luminosity, we measure the luminosities of ≈100 individual water rotational lines at 12–27 μm within the new MIRI spectra. The lines were selected using iSLAT (E. G. Jellison et al. 2023, in preparation) to be spectrally separated from other water lines, as well as from lines from other molecular species known to emit at these wavelengths (OH, HCN, C_2H_2, CO_2, H_2, H I, and Ne II). The selected water lines span E_u between 900 and 10,000 K (black circles in Figure 1). By testing correlations as a function of E_u, we find that the primary correlation with $L_{\rm acc}$ consistently increases with E_u. That is, higher-energy lines correlate more strongly with $L_{\rm acc}$. This is concisely demonstrated in Figure 3 by considering lines in two bins: higher-energy lines with $E_u = 6000$–8000 K (with a correlation coefficient of 0.98) and lower-energy lines with $E_u = 900$–3000 K (with a correlation coefficient of 0.73). To increase the leverage for characterizing the correlation, we also include the high-accretor FZ Tau from Paper I. The correlation in the higher-energy lines is not significantly affected by the removal of the FZ Tau data point (Figure 3). The stronger correlation of water lines from higher E_u is consistent with the scenario where the stellar and accretion irradiation primarily set the emitting area of the hotter, optically thick, inner disk layer (as shown in Appendix C), whereas cooler gas at larger radii may include additional effects from processes linked to ice sublimation near the snow line (as discussed in Section 4). The linear regression of the high-energy line luminosity with accretion luminosity has a slope of ≈0.6, which confirms the value previously found using blended lines at 17.1–17.4 μm from Spitzer-IRS in Banzatti et al. (2020). The deblended lines from a wider range of energy in the MIRI spectra now indicate that the correlation was mostly driven by the higher-energy lines, which indeed dominate the 17.1–17.4 μm water lines (Figure 4).

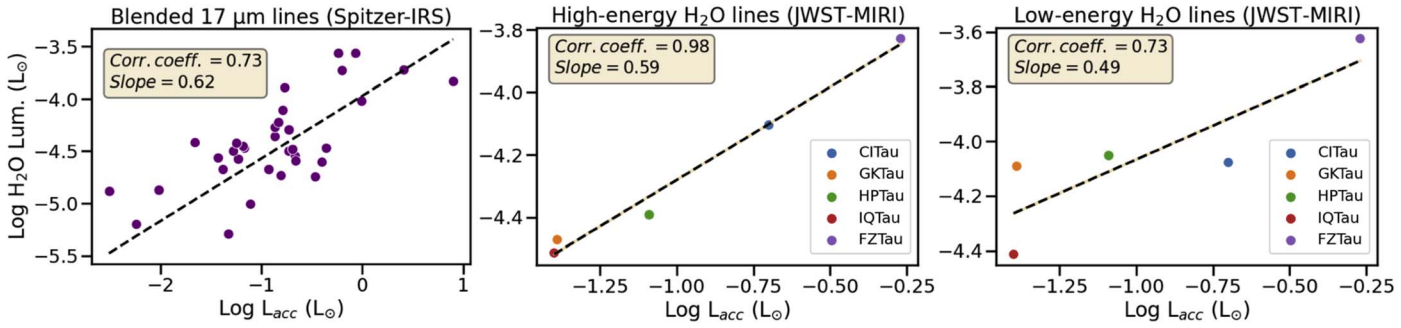

Figure 3. Correlations between water line luminosities and accretion luminosity. Left: using blended water lines at 17.1–17.4 μm from Spitzer-IRS (data and regression adopted from Banzatti et al. 2020). Middle: using high-energy (6000–8000 K) water lines from JWST-MIRI from this work and Paper I. Right: using low-energy (900–3000 K) water lines (see Figure 1).

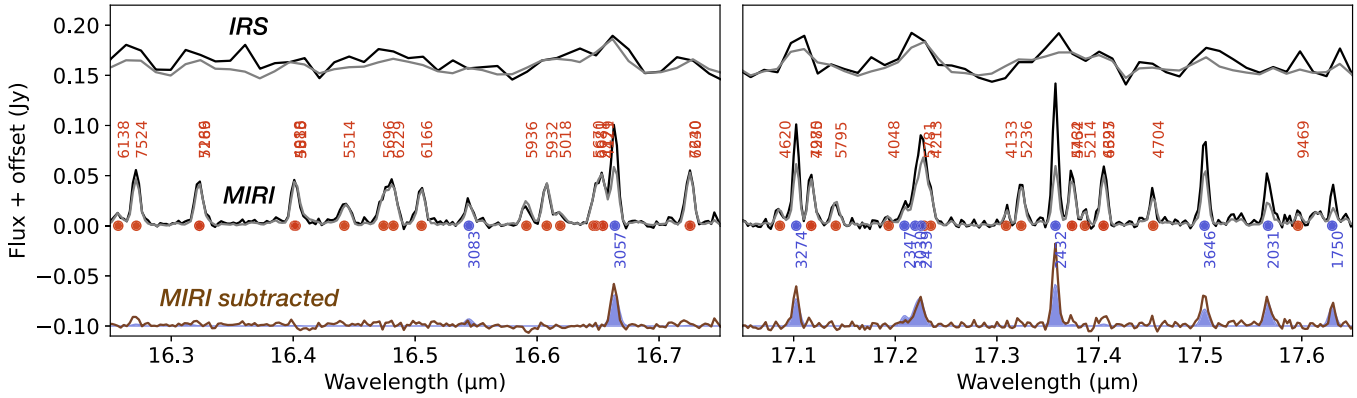

Figure 4. Sections of the continuum-subtracted infrared water spectra of the compact disk GK Tau (in black) and the large disk CI Tau (in gray), at the top from Spitzer-IRS (offset by 0.15 Jy) and in the middle from JWST-MIRI. A broader range of the spectrum is shown in Figure 10 in Appendix B. The CI Tau spectrum is scaled to the distance of GK Tau and corrected for the different accretion luminosity (Section 3). The subtraction of the two spectra is shown in brown at the bottom, with the single-temperature LTE model (blue area) from Figure 5 and Table 2. Vertical labels show the upper level energy E_u in kelvins, separated into higher energy (>4000 K) in red and lower energy (<4000 K) in blue.

In Figure 4, the continuum-subtracted MIRI spectra of GK Tau (compact disk) and CI Tau (large disk with multiple gaps) are compared after scaling CI Tau to the same distance as GK Tau and then applying to CI Tau a scaling factor of 0.42 from the luminosity ratio of the high-energy water lines to remove the line-emitting area dependence on accretion luminosity according to the correlation in Figure 3. The two spectra are then subtracted to obtain the spectral difference in water excitation, revealing that while the relative excitation of high-energy lines is extremely similar in the two disks (after the common scaling factor from the luminosity-dependent emitting area is accounted for), the low-energy lines consistently show some flux excess in the compact disk of GK Tau. The figure also demonstrates that the lower resolution of previous Spitzer spectra did not allow for an unambiguous detection of the cool water excess, although, in hindsight, a slight excess in correspondence of the lower-energy lines may now be identified in the Spitzer-IRS spectrum of GK Tau (Figure 4).

The procedure of scaling and subtracting a template spectrum of a large disk from that of a compact disk is applied systematically to the sample included in this work as visualized in Figure 5. In each column, line luminosities from a compact disk (GK Tau or HP Tau) are divided by those from a large disk (CI Tau or IQ Tau) to obtain the empirical scaling factor between the higher-energy lines tracing the inner hotter emitting region (from the median value of line luminosities between $E_u = 6000$ and 9000 K). The expected scaling factor from applying the linear correlation of the high-energy line luminosities (Figure 3) is shown in orange for reference. The high-energy spectral template is then subtracted, and the line flux of the residuals is fitted with a single-temperature LTE model (Banzatti et al. 2012; Salyk et al. 2011b; Salyk 2020). The excess cool component in the two compact disks is reproduced by an LTE model with rotational temperature $T \approx 400$–500 K, column density $N \approx 1$–5×10^{17} cm^{-2}, and equivalent emitting radius $R_{\rm eq} \approx 0.8$–1 au. The residuals and best-fit solutions are visualized in the rotation diagram in the bottom part of Figure 5.

We note some dependency of the choice of template spectrum on the measured parameters of the cool excess; T is higher, while N and $R_{\rm eq}$ are lower when using IQ Tau as the template instead of CI Tau (second and fourth columns in Figure 5). We interpret this as due to a subtle difference in excitation for the higher-energy lines in the two large disks combined with the intrinsic degeneracies of single-temperature slab model fits (Salyk et al. 2011b; Carr & Najita 2011). Further, the temperature of the cool excess in HP Tau is ≈100 K higher than in GK Tau, possibly as a consequence of differences in the inner disk physical structure, as suggested by the higher infrared index $n_{13\text{–}26}$ in HP Tau.

Lastly, we consider the relations between the properties of the excess cool component and the ALMA dust disk radius in Figure 6. The left panel shows the ratio between the line luminosities of the low- and high-energy water transitions from MIRI. With the four targets analyzed in this work, the correlation coefficient is very high (0.99); this should be more

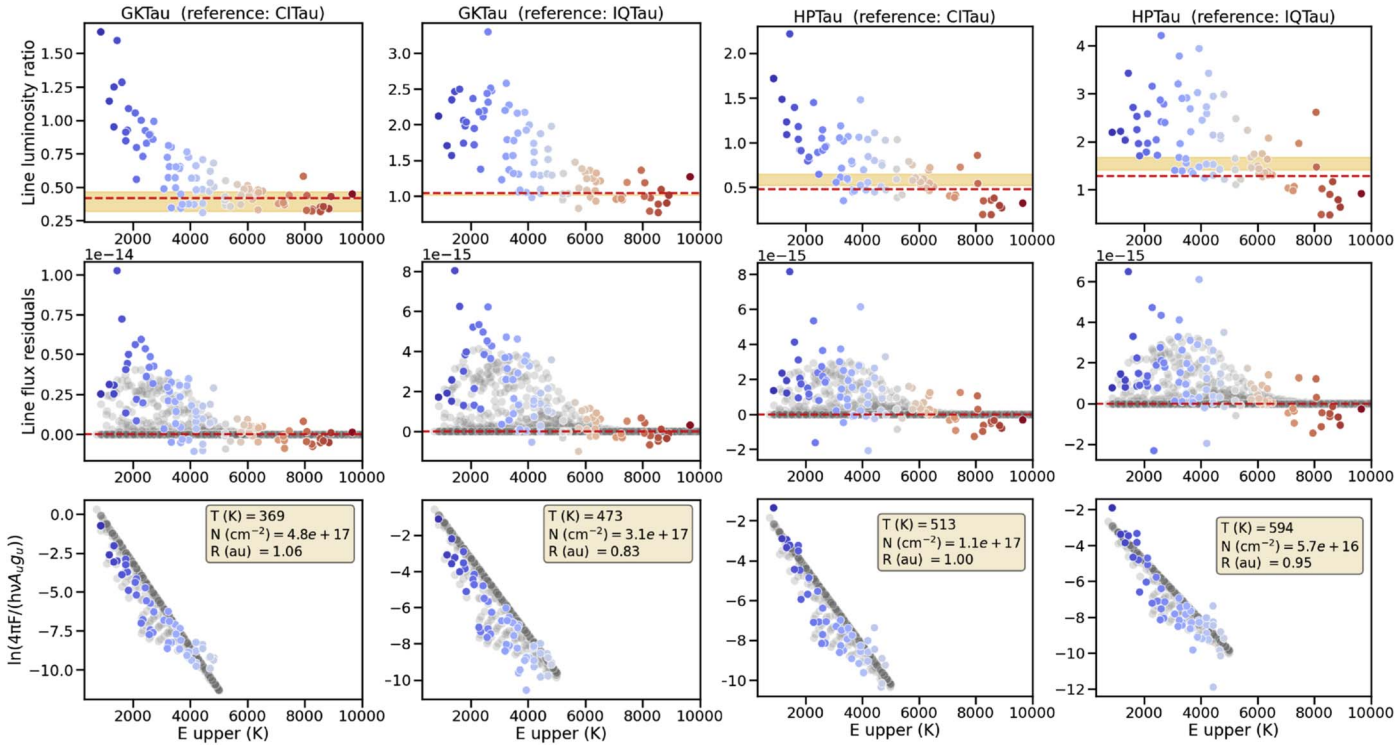

Figure 5. Overview of excess cool components in compact disks by using water spectra in large disks as reference templates for the hotter inner component, as explained in Section 3. The orange area in the top panels is the high-energy line luminosity ratio expected from using the correlation with L_{acc} shown in Figure 3 (3σ region). The red dashed line is the median value of the line luminosity ratio at $E_u \sim 6000$–9000 K. The data point color gradient reflects the E_u value (x-axis) of each water line. A single-temperature LTE fit to line fluxes measured in the excess cool component is shown in gray in the middle (line flux residuals) and bottom (population diagram) panels, with parameters shown in the inset.

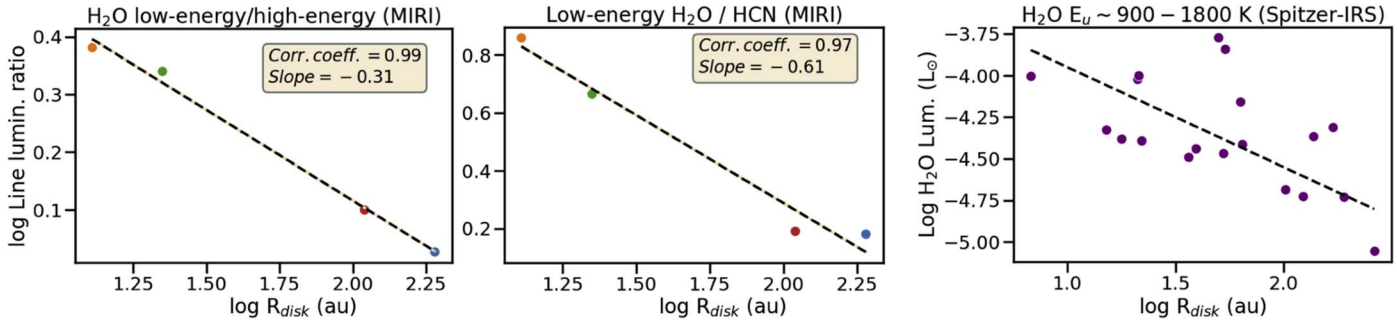

Figure 6. Correlations with dust disk radius R_{disk} for the luminosity ratio between resolved water low- and high-energy lines in MIRI (left), resolved water low-energy lines and the 14 μm HCN band in MIRI (middle), and blended water low-energy lines in Spitzer near 30 μm (taken from Figure 9 in Banzatti et al. 2023, excluding disks with large inner dust cavities).

globally characterized in the future using larger samples. The middle panel shows the ratio between the same low-energy water lines but now using the luminosity of the 14 μm HCN band at the denominator after subtraction of a hot-component water model (Appendix C). This is shown for reference to previous works that measured the H_2O/HCN ratio from Spitzer spectra (Najita et al. 2013; Banzatti et al. 2020). As proposed in Banzatti et al. (2020), the ratio with HCN may work as a normalization factor for H_2O emission, but a change in the O/C elemental ratio may also influence the relative luminosity of H_2O versus organic molecules, which will be analyzed in more detail in future work. In particular, carbon grain destruction near the soot line at ≈500 K (van 't Hoff et al. 2020; Li et al. 2021; Tabone et al. 2023) could result in a different O/C ratio between the regions traced by the hotter (≈800 K) versus colder (≈400 K) water components analyzed in this work.

The right panel shows a previous correlation reported in Banzatti et al. (2023) using low-energy water lines near 30.7 μm from Spitzer spectra. These lines are blends of transitions with $E_u = 900$–1800 K, are well separated from contamination by known OH lines, and were found to have a stronger anticorrelation with the disk radius than the higher-energy Spitzer lines at shorter wavelengths (Banzatti et al. 2023). A reanalysis of archival Spitzer-IRS spectra of GK Tau and CI Tau following the procedure developed above for the MIRI spectra now shows that excess water emission from a temperature consistent with ice sublimation ($T \approx 170$ K) with a large emitting area ($R_{eq} \approx 9$ au) dominates the H_2O lines at >30 μm in the compact disk of GK Tau (Appendix B), with observable flux in MIRI in two low-energy lines at 23.8–23.9 μm, as expected from previous works (Section 1 and

Figure 1). We can therefore conclude with confidence that there is strong evidence from all of the available data, including JWST-MIRI and Spitzer-IRS, for excess cool water vapor in the compact disks as compared to the large disks in this sample.

4. Discussion

In this work, we have analyzed MIRI-MRS spectra of water rotational emission from four protoplanetary disks, two compact ($R_{\rm disk} \approx 10$–20 au) and two large ($R_{\rm disk} \approx 100$–150 au) with multiple dust gaps observed with ALMA, to test previous evidence for enrichment of inner disk water vapor by ice sublimation at the snow line in drift-dominated disks (Banzatti et al. 2020). The analysis shows that the observed higher line luminosity in the compact disks is due to excess flux in the low-energy lines with $E_u < 4000$ K (Figure 4). While all disks share a similar component in the higher-energy lines of optically thick water vapor with $T \approx 800$ K and $N \approx 1 \times 10^{18}$ cm^{-2} (see Appendix C), the compact disks show excess emission consistent with $T \approx 400$ K and $N \approx 1 \times 10^{17}$ cm^{-2} (Section 3), which extends down to at least $T \approx 170$ K when a wider range of lower-energy lines with $E_u < 2000$ K are included, from wavelengths longer than those covered by MIRI-MRS (see Appendix B using Spitzer-IRS). The presence of multiple temperature components probably approximates a temperature gradient—and related radial abundance structure—in the inner disk surface. The existence of a temperature gradient, and in some cases distinct gas reservoirs, is a general prediction of models that include water chemistry and/or transport in planet-forming disks (see references in Section 1). This is consistent with the general gradients previously retrieved using spatially and spectrally unresolved Spitzer and/or Herschel spectra (Blevins et al. 2016; Liu et al. 2019). Within the hotter water emission component, a range of emitting regions and temperatures have been proposed based on spectrally resolved line widths and excitation temperatures that decrease in transitions with an upper level energy range that is currently accessible to high-resolution mid-infrared spectroscopy from the ground (Banzatti et al. 2023).

From the MIRI spectra, the slab model fits reported in this work indicate that the hotter component emits from a more compact region ($R_{\rm eq} \approx 0.5$ au), likely from smaller disk radii, while the excess cooler component traces a more radially extended region ($R_{\rm eq} \gtrsim 1$ au). While large disks may still have weak emission from the cooler region, this work clearly demonstrates that the two compact disks have a significant excess reservoir of cool water vapor, consistent with a larger emitting area. We visualize the proposed approximate radial and vertical location of these different water components in Figure 7. We remark that the moderate resolution of MIRI does not provide direct information on the emitting disk radii for the two water components, only equivalent emitting areas (Section 3); a direct characterization of spatial regions needs higher spatial or spectral resolution from future instrumentation.

The presence of a hot inner water layer may be a common property of gas-rich inner disks around ∼solar-mass young stars as suggested from previous observations with Spitzer-IRS (Salyk et al. 2011b; Carr & Najita 2011). Indeed, the hotter water component in MIRI spectra is found to have a very similar temperature and column density and only a different emitting area in all four disks in this work regardless of their outer dust disk size (Appendix C). The temperature of ≈800 K may represent an average of a temperature gradient extending at least up to ≈1200 K in a more compact inner region at the dust sublimation radius, as suggested by analysis of hot rovibrational water lines (Banzatti et al. 2023). This warm-hot layer is commonly predicted by thermochemical disk models where water vapor forms efficiently through gas-phase chemistry (which is otherwise very inefficient at low temperatures, $T < 300$ K; e.g., Glassgold et al. 2009). These model predictions indeed limit the observed infrared water emission to a surface layer with $T \approx 400$–1000 K and column of $N \approx 10^{18-19}$ cm^{-2} (e.g., Najita & Ádámkovics 2017; Woitke et al. 2018; Anderson et al. 2021; Bosman et al. 2022) in dynamically static scenarios that exclude the effects of radial drift of icy pebbles. The ubiquitous presence of the hot component therefore seems consistent with static chemical models and does not necessarily require enrichment from icy pebbles drifting from the outer disk. The presence of excess cool water emission in the compact disks instead provides an interesting new element to the picture.

What gas reservoir is the excess cool water emission tracing? The large difference in the best-fit emitting areas indicates that the vertical overlap between the hotter and cooler emitting regions is necessarily limited. The cooler water component must be tracing larger radii, rather than just a deeper layer. In fact, while a vertical stack of line emission from a given energy level can produce saturation that may hide cooler emission from closer to the disk midplane, radially distributed line emission will add up in flux without saturation when different temperature components do not share lines of sight. The lower-energy lines also globally have lower Einstein-A coefficients (0.1–10 s^{-1}, compared to 10–100 s^{-1} in the high-energy lines; Figure 1) and therefore naturally trace cooler gas extending to larger radii near and across the snow line (Zhang et al. 2013; Blevins et al. 2016). Radially extended emission in the low-energy lines at temperatures $T \approx 170$–400 K therefore most likely traces a region very close to the ice sublimation front, as ice in disks is indeed expected to sublimate at temperatures $T \approx 120$–180 K (e.g., Pollack et al. 1994; Sasselov & Lecar 2000; Lodders 2003), and vapor is heated up as it diffuses toward hotter disk layers.

Why is this cooler water emission enhanced in compact disks? Kalyaan et al. (2021, 2023) recently presented a series of models investigating the process of inner disk water enrichment from drifting icy solids (Cyr et al. 1998; Ciesla & Cuzzi 2006) in the context of dust gaps and rings revealed by ALMA imaging (Andrews 2020). The models by Kalyaan et al. included both gas and dust evolution, with radially drifting icy solids that progressively sublimate after entering the snow line region, releasing vapor that diffuses inward/upward to enrich the inner disk vapor and outward across the snow line to freeze out again on icy grains (see schematic in Figure 7). They found that inner disk water enrichment is suppressed when a sufficiently deep gap providing an efficient dust trap is present in the disk, particularly when the gap is located at smaller radii close to the snow line, i.e., when it prevents a larger fraction of the outer ice reservoir from reaching the snow line. Disk viscosity is also expected to play a role in regulating pebble drift and inner disk water enrichment, with lower disk viscosities increasing the inner disk water abundance (Schneider & Bitsch 2021; Kalyaan et al. 2023). As the outer dust disk radius shrinks under the effect of inward pebble migration in drift-dominated disks (e.g., Rosotti et al. 2019; Appelgren et al. 2020; Zormpas et al. 2022), an anticorrelation

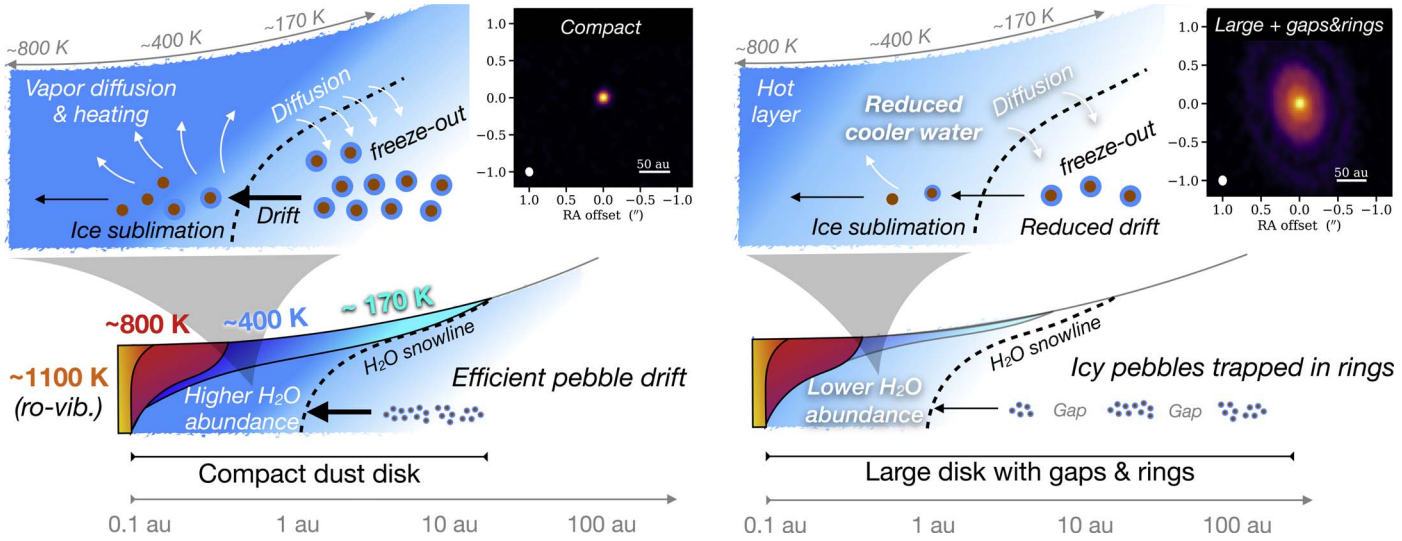

Figure 7. Illustration of the interpretation of the results in the context of the long-proposed scenario of inner water enrichment by pebble drift (Cyr et al. 1998; Ciesla & Cuzzi 2006). The zoomed-in insets show the main processes of pebble drift, ice sublimation, and vapor diffusion as included in recent model explorations by Kalyaan et al. (2021, 2023) in the context of how ice delivery and inner disk water enrichment may be regulated by dust gaps (pebble traps) observed with ALMA.

between inner water enrichment and outer disk radius could indeed be produced as a consequence of icy pebble trapping beyond disk gaps (Figure 10 in Kalyaan et al. 2021). Models also showed that in the absence of drift, a vertical "cold finger effect" could quickly deplete the surface layer above the midplane snow line, both for water and for CO (Meijerink et al. 2009; Krijt et al. 2018), whereas that region would be replenished through ice sublimation and diffusion whenever radial drift is active.

While models propose that it should be the innermost gap to regulate the inner disk water enrichment through pebble drift (Kalyaan et al. 2021), the observed dust disk size is instead set by the location of the outermost gap that retains enough pebbles to be detected with ALMA. The link between the inner disk cool water excess and the outer dust disk size could therefore not necessarily be ubiquitous and depend instead on the number, depth, and location of gaps in disks (Kalyaan et al. 2023). It is worth noting that large disks may have multiple pebble-stopping gaps across a range of disk radii, and this is surely the case for the two large disks included in this work. Object IQ Tau has at least two gaps located at ≈40 and 60 au, and CI Tau has three gaps located at ≈14, 50, and 120 au (Long et al. 2018), as well as possibly an additional gap at 5 au (Jennings et al. 2022b). Moreover, CI Tau has higher-contrast gaps even in comparison to IQ Tau that are likely more efficient in trapping pebbles (e.g., Pinilla et al. 2012), potentially explaining why this is the disk with the lowest cool water excess among the large disks in this work (Figure 6).

While compact disks may have narrow gaps at <30 au that remain unresolved by ALMA, none have been reported for the two compact disks in our sample, even using superresolution techniques (Jennings et al. 2022a, 2022b; Zhang et al. 2023). Further, shallow gaps in inner disks may be very leaky and effectively produce little or no reduction in inner water enrichment (Kalyaan et al. 2023). Future high-resolution dust continuum imaging is needed to better understand the presence of the innermost disk dust gaps and their efficiency in trapping pebbles. While this objective is at the spatial resolution limits of ALMA, it may be possible with a future facility, such as the next-generation Very Large Array (e.g., Andrews et al. 2018). A reduced excess in the cool water reservoir may provide high-priority disk targets for future high-resolution observations to spatially resolve gaps near the snow line at 1–5 au.

In summary, pebble drift and trapping provide a fundamental, natural process for a large-scale link between inner and outer disk regions that may explain the cool water excess revealed by MIRI in the compact disks analyzed in this work. With additional high-resolution data for larger samples, future work will establish how general this effect may be and further establish if pebble drift is indeed the cause of the cool water excess. The specific targets included in this work were observed to test the pebble drift hypothesis by selecting similar-luminosity stars with very different disk sizes (Section 2), with the two large disks having multiple gaps across the disk radii reducing the inward pebble drift (Pinilla et al. 2012). The pebbles are, however, sufficiently large to settle in the disk midplane and cannot be directly observed in the innermost optically thick disk regions, nor can the midplane water vapor mass be directly measured; indeed, the observed surface water would need to be mixed up from the midplane, likely by diffusion and turbulence. While the new observational results from MIRI add evidence that is consistent with water delivery by pebble drift, we consider in the following other scenarios that may offer additional or alternate processes that regulate the inner disk water abundance.

Inner disk dust cavities—The presence of a large inner dust cavity (gaps that extend to the inner dust radius) has been found to likely deplete the abundance of multiple molecules, including water (Salyk et al. 2011b, 2019; Banzatti et al. 2017, 2020, 2022). Yet a small cavity may not have the same effects. All four disks in this paper show CO rovibrational emission tracing hot gas down to within 0.1 au (Appendix A). This demonstrates that there is molecular gas at small radii, without evidence for a gas cavity. The only disk for which the mid-infrared spectral index suggests the presence of an inner dust disk cavity, HP Tau, is a compact disk where the cool water excess is detected. If HP Tau indeed has a <2 au (to be undetected in the ALMA continuum image) gas-rich dust cavity and a midplane snow line of ≈1 au (Table 1), icy pebbles may still drift through the snow line and provide the

cool water excess. A potential alternate explanation for a reduced reservoir of cool water vapor in CI Tau could be if an inner gap at 5 au (Jennings et al. 2022a) is in the region of the surface snow line, and it might be depleting the cool water layer (e.g., by dissociation of H_2O) in addition to reducing pebble drift.

Inner disk gas/dust layers—Could the excess cool water emission be the consequence of a different gas/dust physical structure in compact disks, specifically different gas-to-dust ratios or gas densities? If the compact disks are less dense in their inner regions, we may be detecting cooler water deeper toward the disk midplane. While a deeper layer would not be visible below the optically thick hotter inner water, it might become visible in the less optically thick cooler component. The observability of these layers may also be linked to the relative vertical distribution of gas and dust. In a static disk model, infrared molecular spectra are found to be strongly affected by the gas-to-dust ratio in the emitting layer (e.g., Woitke et al. 2018). In the pebble drift scenario, the dust-to-gas ratio would change in time as a function of the inward drifting pebbles in parallel to the water enrichment (Kalyaan et al. 2021). While molecular line fluxes are generally expected to increase with the decrease of small dust grains in the disk surface (Greenwood et al. 2019), the specific effects of a time-variable dust-to-gas ratio on the observed water spectrum (including the layer depth for different temperature components) will require dedicated future work to be quantified.

Disk surface accretion—Surface accretion flows may offer an alternate way to transport water to inner disk atmospheres. In contrast to pebble accretion, in which icy material close to the disk midplane flows inward rapidly relative to the gas, small icy grains near the disk surface can flow inward as part of the general accretion flow that transports gas and dust through the disk toward the star. While surface flows deliver water in the form of well-mixed small icy grains, this process will not enrich water over the primordial baseline, but it may replenish observable surface water lost by freeze-out and settling to the midplane. The idea of surface accretion dates back at least to the layered accretion picture of Gammie (1996), in which only the surface region of the disk is ionized enough to couple to magnetic fields, lose angular momentum, and thereby accrete toward the star. Surface accretion flows at supersonic velocities are predicted in recent MHD simulations of magnetized disks (e.g., Bai & Stone 2013; Bai 2017; Zhu & Stone 2018) and may increase the temperature contrast between the disk surface and midplane (Mori et al. 2019), which could also have an effect on the observed gas emission. Although such gas flows in disks may be difficult to observe, observational evidence for supersonic surface accretion has been reported in at least one system: an edge-on disk system, where the favorable inclination renders the surface flow more readily observable (Najita et al. 2021). The reason compact disks may have enhanced surface accretion in comparison to large disks, to potentially explain the excess cool emission found in this work, is, however, currently unclear.

Other scenarios—A number of other scenarios could be considered as possibly playing a role, including (i) if inner disk turbulence or diffusion is, for some reason, enhanced in compact disks, it might produce a larger cool water layer by mixing cool water higher up in the disk surface, or (ii) planetesimal formation could perhaps trap icy solids from drifting inside the snow line region (Najita et al. 2013), although modeling work suggests that this effect should be minor in comparison to pebble trapping by gaps (Kalyaan et al. 2023). The discovery of the cool water excess with MIRI opens up interesting prospects for testing and validating these different scenarios with future modeling work.

5. Summary and Future Prospects

This work reports molecular spectra observed with MIRI-MRS in four protoplanetary disks in Taurus, two compact disks (10–20 au) and two large disks (100–150 au) with multiple dust gaps observed with ALMA. The comparative analysis of these spectra, using the two large-structured disks as templates for water emission, reveals that the compact disks have excess water emission in the lower-energy lines. We summarize our conclusions as follows.

1. The excitation of higher-energy ($E_u > 4000$ K) rotational water lines in all four disks is very similar after accounting for the dependence of the emitting area on accretion luminosity. This hotter, inner reservoir ($T \approx 800$ K and $R_{eq} \approx 0.5$ au) is optically thick ($N \approx 1 \times 10^{18}$ cm^{-2}) and common across the sample as predicted by static thermochemical models that assume water formation through gas-phase reactions.
2. The excess emission in lower-energy water lines ($E_u < 4000$ K) in the compact disks is well approximated by LTE models with $T \approx 170$–400 K and $R_{eq} \approx 1$–10 au, therefore most likely tracing a disk region very close to ice sublimation at the water snow line. This excess emission was likely driving the correlations discovered in previous work using spectrally blended Spitzer-IRS data (Najita et al. 2013; Banzatti et al. 2020).
3. The excess cool water emission naturally fits into fundamental predictions of inner disk water enrichment through sublimation of drifting icy pebbles that cross the snow line (Cyr et al. 1998; Ciesla & Cuzzi 2006; Kalyaan et al. 2021, 2023). This scenario predicts that compact disks do not have deep gaps outside the snow line to prevent pebble drift from enriching the inner disk with abundant water vapor, whereas large disks retain a large fraction of pebbles in the outer disk and decrease the inward delivery of ice. Other processes that may regulate the cool water layer to explore in the future include a varying gas-to-dust ratio (in time and/or disk layer), the removal of water by disk gaps near the snow line, or hypothetically a different surface gas accretion in different disks.

The findings of this work open up a number of exciting prospects. While this work includes the first four spectra from program GO-1640, which was set up with the specific goal of studying water emission in connection to pebble drift, a large number of disk spectra will be observed with MIRI in Cycle 1 and future cycles. The larger sample will soon enable investigations of how common the cool water excess is, how it varies with disk size and the location and depth of dust gaps, and how it may vary with other parameters like stellar mass and luminosity, age and environment, or the formation of inner disk cavities. In particular, the location and depth of the innermost disk gaps—which should be studied in larger samples with the highest-resolution interferometric images—may be fundamental in regulating inner disk water enrichment (as proposed in Kalyaan et al. 2023) and reflected in variations in the

temperature, density, and radial location of the cool water excess.

Another exciting prospect is the investigation of how molecular chemistry more generally and the elemental C/H, O/H, and N/H ratios are affected by pebble drift and inner disk water enrichment using the organics detected in disks (e.g., Figure 11). MIRI spectra will enable future tests of a number of models that provide predictions on how molecular chemistry may be affected across snow lines depending on the drift and trapping or sublimation of icy particles (e.g., Pinilla et al. 2017; Booth & Ilee 2019; Müller et al. 2021; Notsu et al. 2022; Cevallos Soto et al. 2022), helping to increase our understanding of inner disk regions that are considered fundamental for planet formation (e.g., Drażkowska et al. 2023; Krijt et al. 2023). If icy pebble drift is indeed regulating the cool water reservoir observed with MIRI, the infrared water spectrum could be used in the future to estimate the pebble mass flux and water ice delivered to the snow line region, which will inform models of the solid mass available for the formation of planetesimals, terrestrial planets, and giant planet cores (e.g., Lambrechts et al. 2019; Bitsch et al. 2019a) and connecting disk observations to the architecture and chemical composition of planetary system that may be forming in them (e.g. Cridland et al. 2016; Bitsch et al. 2019b; van der Marel & Mulders 2021). Future high-resolution spectroscopy at mid- to far-infrared wavelengths, beyond the MIRI-MRS cutoff at 28 μm, will be required to more comprehensively study the cool water component down to 150 K and possibly cooler temperatures across and beyond the snow line region (Notsu et al. 2016; Pontoppidan et al. 2018; Kamp et al. 2021).

Acknowledgments

This work is based on observations made with the NASA/ESA/CSA James Webb Space Telescope. The JWST data used in this paper can be found in MAST: https://doi.org/10.17909/rjt1-jd72. The data were obtained from the Mikulski Archive for Space Telescopes at the Space Telescope Science Institute, which is operated by the Association of Universities for Research in Astronomy, Inc., under NASA contract NAS 5-03127 for JWST. The observations are associated with JWST GO Cycle 1 programs 1549 and 1640. This work has made use of data from the European Space Agency (ESA) mission Gaia (https://www.cosmos.esa.int/gaia), processed by the Gaia Data Processing and Analysis Consortium (DPAC; https://www.cosmos.esa.int/web/gaia/dpac/consortium). Funding for the DPAC has been provided by national institutions, in particular the institutions participating in the Gaia Multilateral Agreement. A portion of this work was carried out at the Jet Propulsion Laboratory, California Institute of Technology, under a contract with the National Aeronautics and Space Administration. This paper makes use of the following ALMA data: ADS/JAO.2016.1.01164.S. ALMA is a partnership of ESO (representing its member states), NSF (USA) and NINS (Japan), together with NRC (Canada), MOST and ASIAA (Taiwan), and KASI (Republic of Korea), in cooperation with the Republic of Chile. The Joint ALMA Observatory is operated by ESO, AUI/NRAO and NAOJ. We thank the anonymous reviewer for suggestions that helped improve this manuscript. A.B. and A.K. acknowledge support from NASA/Space Telescope Science Institute grant JWST-GO-01640. I.P. acknowledges partial support by NASA under agreement No. 80NSSC21K0593 for the program "Alien Earths." Support for F.L. was provided by NASA through the NASA Hubble Fellowship grant No. HST-HF2-51512.001-A awarded by the Space Telescope Science Institute, which is operated by the Association of Universities for Research in Astronomy, Incorporated, under NASA contract NAS5-26555. G.R. is funded by the European Union (ERC Starting Grant DiscEvol, project No. 101039651). The views and opinions expressed are, however, those of the author(s) only and do not necessarily reflect those of the European Union or the European Research Council Executive Agency. Neither the European Union nor the granting authority can be held responsible for them. A.B. thanks Tommy for helping him to rediscover cold water.

Software: Matplotlib (Hunter 2007), NumPy (van der Walt et al. 2011), SciPy (Virtanen et al. 2020), Seaborn (Waskom 2021).

Appendix A
Ground-based Data for the Sample

Figure 8 shows the ALMA images for all four disks included in this work, from Long et al. (2019). Figure 9 reports high-resolution ($R \sim 60{,}000$–$90{,}000$, or 3–5 km s^{-1}) line profiles for the CO fundamental band ($\nu = 1$–0) as observed from the ground with iSHELL (Rayner et al. 2022) as part of an ongoing disk survey (Banzatti et al. 2022; with GK Tau and HP Tau observed on 2023 February 15, just 12 days before the MIRI spectra analyzed in this work) and CRIRES (Kaeufl et al. 2004) as part of a previous survey (IQ Tau as observed in 2008; Pontoppidan et al. 2011; Brown et al. 2012). The CO kinematics, which trace a similar range of inner disk regions as the infrared water lines (Banzatti et al. 2023), demonstrate that CO spans similar disk radii in these four disks around 0.1 au (in Table 1, we report the Keplerian radii from the measured velocities at 10% and 50% of the CO line width). Some notable differences are visible in IQ Tau (showing more compact emission) and HP Tau (showing more extended emission). All four disks show narrow CO absorption at low velocities that might be due to absorption in cold foreground gas or self-absorption in a cooler molecular inner disk wind above the disk surface (Pontoppidan et al. 2011; Banzatti et al. 2022; the absorption is detected only up to P4 in GK Tau and therefore not visible in Figure 9).

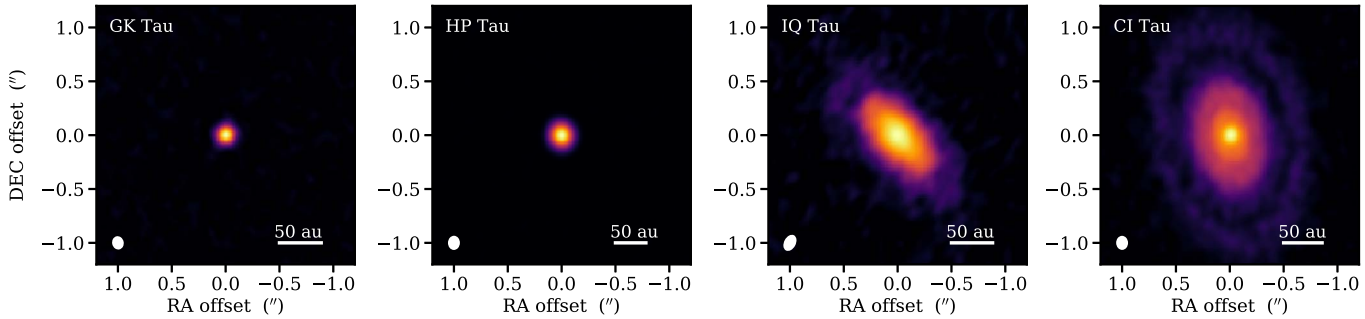

Figure 8. ALMA images for the sample ordered by disk radius from Long et al. (2019).

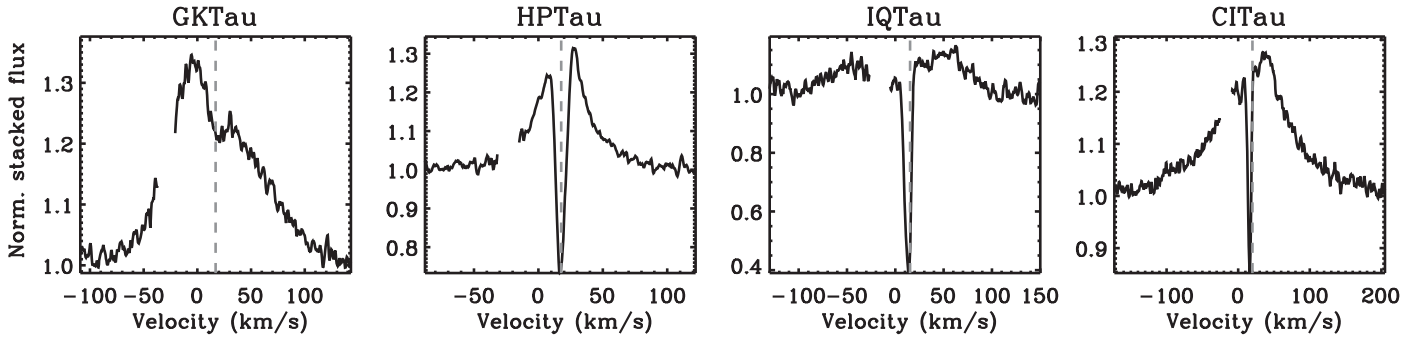

Figure 9. Stacked P5–P18 line profiles of CO rovibrational fundamental emission observed in the four targets from iSHELL and CRIRES spectra in Banzatti et al. (2022), Brown et al. (2012), and this work. The stellar RV is marked with a dashed line, and the gaps on the blue side of each line are due to telluric lines at the time of observation.

Appendix B
Broader Spectral Characterization of Excess Cool Component

To obtain a more comprehensive view of the cool excess component in compact disks, we include the Spitzer-IRS spectra of CI Tau and GK Tau from Pontoppidan et al. (2010a) and Banzatti et al. (2020). Object HP Tau was never observed with IRS, and IQ Tau only has a lower-quality spectrum with higher noise (James et al. 2022). As shown in Zhang et al. (2013) and Blevins et al. (2016), cool water emission from the snow line at $T \approx 150$ K should dominate the observed water spectrum at 30–70 μm, beyond the MIRI range but partly covered by IRS (see Figure 1). We apply to the IRS spectra the same scaling and subtraction procedure developed on the MIRI spectra (Section 3) and refit the excess emission in GK Tau at MIRI and IRS wavelengths with a two-temperature model to approximately account for a radial temperature gradient that is expected at the disk radii across the snow line (1–10 au; Blevins et al. 2016). The fit is shown in Figure 10. The two components have $T \approx 420$ K, $N \approx 3.5 \times 10^{17}$ cm^{-2}, and $R_{\rm eq} \approx 0.9$ au (best-fit values that are essentially unchanged from fitting the excess in the MIRI spectrum alone, as reported in Section 3) and $T \approx 170$ K, $N \approx 3 \times 10^{16}$ cm^{-2}, and $R_{\rm eq} \approx 9$ au. The colder of these two components emits most prominently at >30 μm, as found before (Zhang et al. 2013; Blevins et al. 2016), but the IRS spectra alone would leave large uncertainties on its presence and properties. The new MIRI data analyzed in this work instead enable the identification of the 170 K component by deblending individual lines (just like it was shown in Figure 4 for the separation of the $T \approx 800$ and 400 K components); two prominent MIRI lines at 23.81 and 23.89 μm clearly show excess that could not be fitted with the rest of the excess spectrum using a single temperature of $T \approx 400$ K (see also the excess flux in the lowest-energy lines in middle panels in Figure 5), and their excess flux is now filled in by the extra cool component at $T \approx 170$ K (Figure 10). From Figure 6 in Zhang et al. (2013), we can see that this was to be expected; these two lines are as sensitive to the abundance and radial distribution of water across the snow line as the lines at 30 μm (covered by IRS) and 60–70 μm (covered by Herschel-PACS), which indeed all share similar properties, $E_u \approx 1000$ K and $A_{ul} \approx 1$–10 s^{-1}.

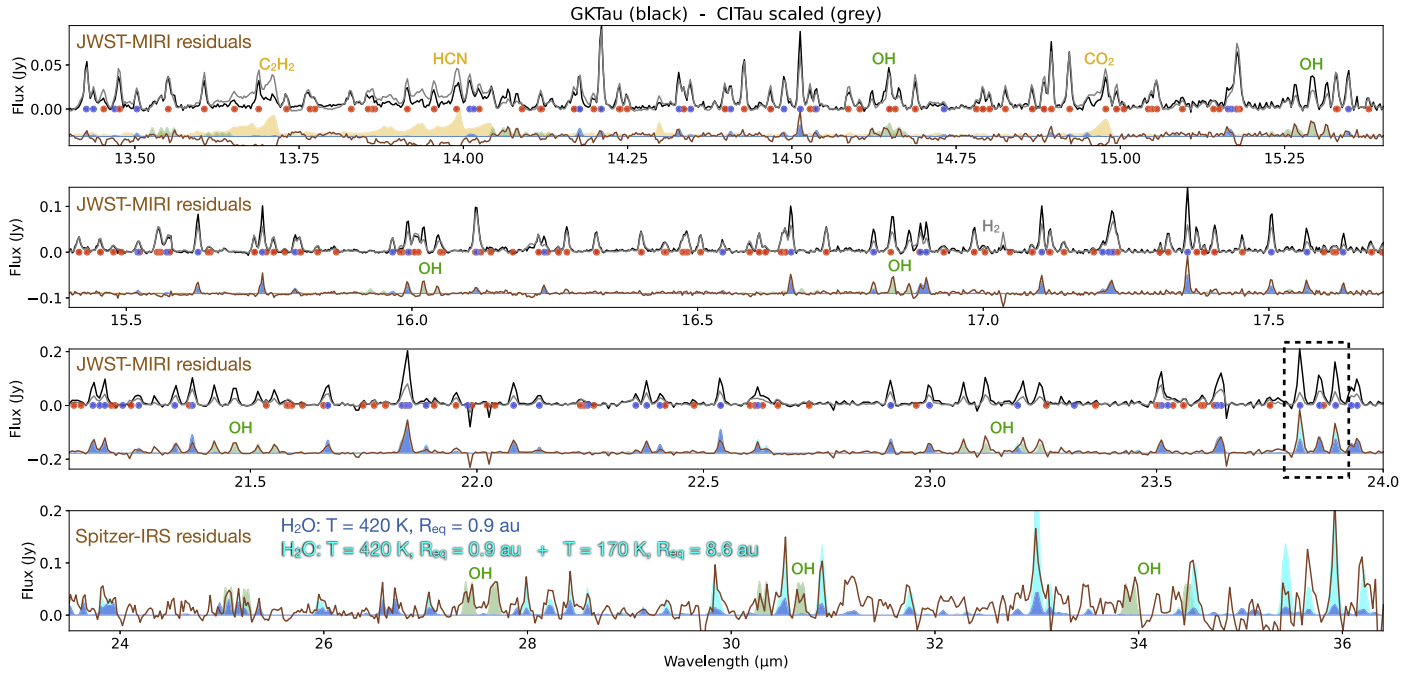

Figure 10. Broader view of the excess cool component in rotational water emission in GK Tau, using CI Tau as a template for the hot component as in Figure 4. The same scaling and subtraction procedure described in Section 3 is applied here, where residuals after subtraction are shown in brown for MIRI (top three panels) and IRS (bottom panel). A two-temperature fit is shown in blue (only the $T \approx 400$ K component) and cyan (the $T \approx 400$ and 170 K components together), with best-fit values as reported in Appendix B. The dashed box marks the two MIRI lines discussed in the text. Other molecules are reported and labeled in different colors for reference.

Appendix C
Single-temperature Fits to the High-energy Lines

For comparison to the properties of the excess cool component, we also fit a single-temperature LTE model to the higher-energy water lines that dominate the emission at 12–16 μm. The best-fit parameters cluster around $T \approx 830$ K, $N \approx 1 \times 10^{18}$ cm^{-2}, and equivalent emitting radius $R_{\rm eq} \approx 0.5$ au and are reported in Table 2 and Figure 11. At this column density, the high-energy water lines at these wavelengths are moderately optically thick with an opacity at the line center of $\tau \approx 0.2$–10 (for the definition of τ, see the Appendix in Banzatti et al. 2012). The best-fit emitting areas confirm what is reported in Section 3 about the high-energy lines mostly tracing a luminosity-dependent optically thick emitting area in different disks, with CI Tau having the largest emitting area with $R_{\rm eq} \approx 0.65$ au and the other three disks having similar emitting areas with $R_{\rm eq} \approx 0.4$ au. The $L_{\rm acc}$ ratio between CI Tau and the other three disks is ≈2.5–5, which, elevated to the power of 0.6 (the slope of the correlation in Figure 3), gives ≈1.7–2.6, fully consistent with the emitting area ratio of ≈2.1 from the slab fits.

The best-fit values found for the hot component are consistent with LTE fits to spectrally resolved water emission lines near 12.4 μm from ground-based observations (Banzatti et al. 2023) and recent fits to a similar range of MIRI water lines in another disk (Grant et al. 2023). A single temperature in LTE is generally sufficient to provide a good fit in this limited wavelength range, as found before with Spitzer and MIRI spectra (Carr & Najita 2011; Banzatti et al. 2012; Grant et al. 2023), but fitting larger ranges requires at least a temperature gradient (Blevins et al. 2016; Liu et al. 2019; Banzatti et al. 2023). For reference, we report that preliminary two-temperature LTE fits to the whole range of rotational lines in the MIRI spectra of the four disks analyzed in this work are also consistent with the two temperatures reported in this work, a hot component with $T \approx 800$–1000 K and a cool one with $T \approx 200$–400 K. Previous work suggested that the gas density in the water-emitting layer is below the critical density $n_{\rm crit}$ necessary to thermalize infrared water lines, especially at higher upper level energies of $E_u > 4000$ K (Meijerink et al. 2009), with rotational lines having $n_{\rm crit} \approx 10^{8-11}$ cm^{-3} and the rovibrational bands having $n_{\rm crit} \approx 10^{12-16}$ cm^{-3}. This should produce non-LTE populations of the higher energy levels, which should be most visible in the rovibrational bands (Bosman et al. 2022), explaining a strong flux reduction that

Table 2
LTE Model Fits to Rotational Water Lines

Object	H_2O High Energy			H_2O Low-energy Excess		
	$R_{\rm eq}$ (au)	T (K)	log N (cm^{-2})	$R_{\rm eq}$ (au)	T (K)	log N (cm^{-2})
CI Tau	0.65	840	1.0e18	…	…	…
IQ Tau	0.38	850	1.1e18	…	…	…
HP Tau	0.46	820	1.1e18	1.00	510	1.1e17
GK Tau	0.45	830	7.1e17	1.06	370	4.8e17
GK Tau[a]	…	…	…	0.87	420	3.5e17
GK Tau[a]	…	…	…	8.6	170	3.1e16

Note. See Section 3 for details on the separation of components. For the high-energy component, we report fit results to the 12–16 μm range from Appendix C. For the cool excess component, we report results obtained by using the spectrum of CI Tau as a template for the inner hot component (see Figure 5). While IQ Tau shows some cool excess in comparison to CI Tau (Figure 6), it is too weak for the fit to converge.
[a] Results from the two-temperature fit to MIRI and IRS residuals reported in Appendix B.

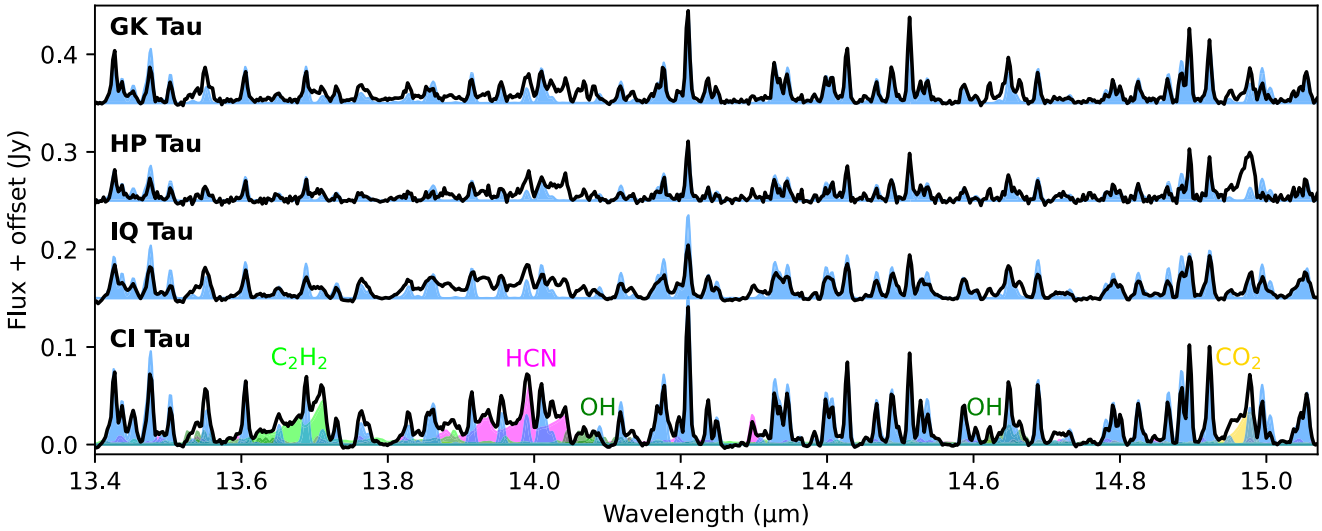

Figure 11. Single-temperature LTE fits to the high-energy lines that dominate water spectra at 12–16 μm. Best-fit parameters are reported in Table 2. Representative models of organics and OH emission are reported for reference at the bottom.

has indeed been observed (Banzatti et al. 2023); the rotational lines with higher E_u may also be reduced by factors of a few (Meijerink et al. 2009; Banzatti et al. 2012). The increased resolution of MIRI now better shows a residual mismatch with the LTE models, which are currently being investigated in terms of non-LTE excitation and will be reported in a future paper in combination with the analysis of the rovibrational band at <9 μm.

ORCID iDs

Andrea Banzatti https://orcid.org/0000-0003-4335-0900
Klaus M. Pontoppidan https://orcid.org/0000-0001-7552-1562
John S. Carr https://orcid.org/0000-0002-6695-3977
Ilaria Pascucci https://orcid.org/0000-0001-7962-1683
Joan R. Najita https://orcid.org/0000-0002-5758-150X
Carlos E. Muñoz-Romero https://orcid.org/0000-0001-7152-9794
Karin I. Öberg https://orcid.org/0000-0001-8798-1347
Anusha Kalyaan https://orcid.org/0000-0002-5067-1641
Paola Pinilla https://orcid.org/0000-0001-8764-1780
Sebastiaan Krijt https://orcid.org/0000-0002-3291-6887
Feng Long https://orcid.org/0000-0002-7607-719X
Giovanni Rosotti https://orcid.org/0000-0003-4853-5736
Gregory J. Herczeg https://orcid.org/0000-0002-7154-6065
Colette Salyk https://orcid.org/0000-0003-3682-6632
Ke Zhang https://orcid.org/0000-0002-0661-7517
Edwin A. Bergin https://orcid.org/0000-0003-4179-6394
Nicholas P. Ballering https://orcid.org/0000-0002-4276-3730
Michael R. Meyer https://orcid.org/0000-0003-1227-3084

References

Anderson, D. E., Blake, G. A., Cleeves, L. I., et al. 2021, ApJ, 909, 55
Andrews, S. M. 2020, ARA&A, 58, 483
Andrews, S. M., Wilner, D. J., Macías, E., Carrasco-González, C., & Isella, A. 2018, in ASP Conf. Ser. 517, Science with a Next Generation Very Large Array, ed. E. Murphy (San Francisco, CA: ASP), 137
Appelgren, J., Lambrechts, M., & Johansen, A. 2020, A&A, 638, A156
Bae, J., Isella, A., Zhu, Z., et al. 2022, arXiv:2210.13314
Bai, X.-N. 2017, ApJ, 845, 75
Bai, X.-N., & Stone, J. M. 2013, ApJ, 769, 76
Banzatti, A. 2013, PhD thesis, Eidgenossische Technische Hochschule, Zurich, Switzerland
Banzatti, A., Abernathy, K. M., Brittain, S., et al. 2022, AJ, 163, 174
Banzatti, A., Meyer, M. R., Bruderer, S., et al. 2012, ApJ, 745, 90
Banzatti, A., Pascucci, I., Bosman, A. D., et al. 2020, ApJ, 903, 124
Banzatti, A., Pontoppidan, K. M., Pére Chávez, J., et al. 2023, AJ, 165, 72
Banzatti, A., Pontoppidan, K. M., Salyk, C., et al. 2017, ApJ, 834, 152
Bitsch, B., Izidoro, A., Johansen, A., et al. 2019a, A&A, 623, A88
Bitsch, B., Raymond, S. N., & Izidoro, A. 2019b, A&A, 624, A109
Blevins, S. M., Pontoppidan, K. M., Banzatti, A., et al. 2016, ApJ, 818, 22
Booth, R. A., & Ilee, J. D. 2019, MNRAS, 487, 3998
Bosman, A. D., Bergin, E. A., Calahan, J., & Duval, S. E. 2022, ApJL, 930, L26
Bosman, A. D., Bruderer, S., & van Dishoeck, E. F. 2017, A&A, 601, A36
Brown, J. M., Herczeg, G. J., Pontoppidan, K. M., & van Dishoeck, E. F. 2012, ApJ, 744, 116
Carr, J. S., & Najita, J. R. 2008, Sci, 319, 1504
Carr, J. S., & Najita, J. R. 2011, ApJ, 733, 102
Cevallos Soto, A., Tan, J. C., Hu, X., Hsu, C.-J., & Walsh, C. 2022, MNRAS, 517, 2285
Ciesla, F. J., & Cuzzi, J. N. 2006, Icar, 181, 178
Clarke, C. J., Tazzari, M., Juhasz, A., et al. 2018, ApJL, 866, L6
Cridland, A. J., Pudritz, R. E., Alessi, M., et al. 2016, MNRAS, 461, 3274
Cridland, A. J., van Dishoeck, E. F., Alessi, M., & Pudritz, R. E. 2019, A&A, 632, A63
Cyr, K. E., Sears, W. D., & Lunine, J. I. 1998, Icar, 135, 537
Donati, J. F., Bouvier, J., Alencar, S. H., et al. 2020, MNRAS, 491, 5660
Drażkowska, J., Bitsch, B., Lambrechts, M., et al. 2023, in ASP Conf. Ser. 534, Astronomical Society of the Pacific Conference Series, ed. S. Inutsuka et al. (San Francisco, CA: ASP), 717
Feiden, G. A. 2016, A&A, 593, A99
Gaia Collaboration, Prusti, T., de Bruijne, J. H. J., et al. 2016, A&A, 595, A1
Gaia Collaboration, Vallenari, A., Brown, A. G. A., et al. 2022, A&A, 674, A1
Gammie, C. F. 1996, ApJ, 457, 355
Gangi, M., Antoniucci, S., Biazzo, K., et al. 2022, A&A, 667, A124
Gardner, J. P., Mather, J. C., Abbott, R., et al. 2023, PASP, 135, 068001
Gasman, D., van Dishoeck, E. F., Grant, S. L., et al. 2023, arXiv:2307.09301
Glassgold, A. E., Meijerink, R., & Najita, J. R. 2009, ApJ, 701, 142
Grant, S. L., van Dishoeck, E. F., Tabone, B., et al. 2023, ApJL, 947, L6
Greenwood, A. J., Kamp, I., Waters, L. B. F. M., Woitke, P., & Thi, W. F. 2019, A&A, 631, A81
Herczeg, G. J., & Hillenbrand, L. A. 2014, ApJ, 786, 97
Houck, J. R., Roellig, T. L., van Cleve, J., et al. 2004, ApJS, 154, 18
Hunter, J. D. 2007, CSE, 9, 90
Ida, S., Guillot, T., & Morbidelli, A. 2016, A&A, 591, A72
James, M. M., Pascucci, I., Liu, Y., et al. 2022, ApJ, 941, 187
Jennings, J., Booth, R. A., Tazzari, M., Clarke, C. J., & Rosotti, G. P. 2022a, MNRAS, 509, 2780

Jennings, J., Tazzari, M., Clarke, C. J., Booth, R. A., & Rosotti, G. P. 2022b, MNRAS, 514, 6053
Kaeufl, H.-U., Ballester, P., Biereichel, P., et al. 2004, Proc. SPIE, 5492, 1218
Kalyaan, A., Pinilla, P., Krijt, S., et al. 2023, ApJ, 954, 66
Kalyaan, A., Pinilla, P., Krijt, S., Mulders, G. D., & Banzatti, A. 2021, ApJ, 921, 84
Kamp, I., Honda, M., Nomura, H., et al. 2021, PASA, 38, e055
Krijt, S., Kama, M., McClure, M., et al. 2023, in ASP Conf. Ser. 534, Protostars and Planets VII, ed. S. Inutsuka et al. (San Francisco, CA: ASP), 1031
Krijt, S., Schwarz, K. R., Bergin, E. A., & Ciesla, F. J. 2018, ApJ, 864, 78
Labiano, A., Argyriou, I., Álvarez-Márquez, J., et al. 2021, A&A, 656, A57
Lambrechts, M., & Johansen, A. 2012, A&A, 544, A32
Lambrechts, M., Morbidelli, A., Jacobson, S. A., et al. 2019, A&A, 627, A83
Levison, H. F., Kretke, K. A., Walsh, K. J., & Bottke, W. F. 2015, PNAS, 112, 14180
Li, J., Bergin, E. A., Blake, G. A., Ciesla, F. J., & Hirschmann, M. M. 2021, SciA, 7, eabd3632
Liu, Y., Pascucci, I., & Henning, T. 2019, A&A, 623, A106
Lodders, K. 2003, ApJ, 591, 1220
Long, F., Herczeg, G. J., Harsono, D., et al. 2019, ApJ, 882, 49
Long, F., Pinilla, P., Herczeg, G. J., et al. 2018, ApJ, 869, 17
Manara, C. F., Ansdell, M., Rosotti, G. P., et al. 2023, in ASP Conf. Ser. 534, Protostars and Planets VII, ed. S.-i. Inutsuka et al. (San Francisco, CA: ASP), 539
Meijerink, R., Pontoppidan, K. M., Blake, G. A., Poelman, D. R., & Dullemond, C. P. 2009, ApJ, 704, 1471
Morfill, G. E., & Voelk, H. J. 1984, ApJ, 287, 371
Morbidelli, A., Bitsch, B., Crida, A., et al. 2016, Icar, 267, 368
Mori, S., Bai, X.-N., & Okuzumi, S. 2019, ApJ, 872, 98
Mulders, G. D., Ciesla, F. J., Min, M., & Pascucci, I. 2015, ApJ, 807, 9
Müller, J., Savvidou, S., & Bitsch, B. 2021, A&A, 650, A185
Najita, J. R., & Ádámkovics, M. 2017, ApJ, 847, 6
Najita, J. R., Ádámkovics, M., & Glassgold, A. E. 2011, ApJ, 743, 147
Najita, J. R., Carr, J. S., Brittain, S. D., et al. 2021, ApJ, 908, 171
Najita, J. R., Carr, J. S., Pontoppidan, K. M., et al. 2013, ApJ, 766, 134
Najita, J. R., Carr, J. S., Salyk, C., et al. 2018, ApJ, 862, 122
Notsu, S., Nomura, H., Ishimoto, D., et al. 2016, ApJ, 827, 113
Notsu, S., Ohno, K., Ueda, T., et al. 2022, ApJ, 936, 188
Pascucci, I., Herczeg, G., Carr, J. S., & Bruderer, S. 2013, ApJ, 779, 178
Pinilla, P., Benisty, M., & Birnstiel, T. 2012, A&A, 545, A81
Pinilla, P., Pohl, A., Stammler, S. M., & Birnstiel, T. 2017, ApJ, 845, 68
Pollack, J. B., Hollenbach, D., Beckwith, S., et al. 1994, ApJ, 421, 615
Pontoppidan, K. M., Bergin, E. A., Melnick, G., et al. 2018, arXiv:1804.00743
Pontoppidan, K. M., Blake, G. A., & Smette, A. 2011, ApJ, 733, 84
Pontoppidan, K. M., Salyk, C., Bergin, E. A., et al. 2014, in Protostars and Planets VI, ed. H. Beuther et al. (Tucson, AZ: Univ. of Arizona Press), 363
Pontoppidan, K. M., Salyk, C., Blake, G. A., et al. 2010a, ApJ, 720, 887
Pontoppidan, K. M., Salyk, C., Blake, G. A., & Käufl, H. U. 2010b, ApJL, 722, L173
Pontoppidan, K. M., Salyk, C., Banzatti, A., et al. 2023, ApJ, submitted
Rayner, J., Tokunaga, A., Jaffe, D., et al. 2022, PASP, 134, 015002
Rieke, G. H., Wright, G. S., Böker, T., et al. 2015, PASP, 127, 584
Rosotti, G. P., Tazzari, M., Booth, R. A., et al. 2019, MNRAS, 486, 4829
Salyk, C. 2020, slabspec: Python code for producing LTE slab model molecular spectra, v1.0.0, Zenodo, doi:10.5281/zenodo.4037306
Salyk, C., Blake, G. A., Boogert, A. C. A., & Brown, J. M. 2011a, ApJ, 743, 112
Salyk, C., Lacy, J., Richter, M., et al. 2019, ApJ, 874, 24
Salyk, C., Pontoppidan, K. M., Blake, G. A., et al. 2008, ApJL, 676, L49
Salyk, C., Pontoppidan, K. M., Blake, G. A., Najita, J. R., & Carr, J. S. 2011b, ApJ, 731, 130
Sasselov, D. D., & Lecar, M. 2000, ApJ, 528, 995
Schneider, A. D., & Bitsch, B. 2021, A&A, 654, A71
Stevenson, D. J., & Lunine, J. I. 1988, Icar, 75, 146
Tabone, B., Bettoni, G., van Dishoeck, E. F., et al. 2023, NatAs, 7, 805
van der Marel, N., & Mulders, G. D. 2021, AJ, 162, 28
van der Walt, S., Colbert, S. C., & Varoquaux, G. 2011, CSE, 13, 22
van 't Hoff, M. L. R., Bergin, E. A., Jørgensen, J. K., & Blake, G. A. 2020, ApJL, 897, L38
Virtanen, P., Gommers, R., Oliphant, T. E., et al. 2020, NatMe, 17, 261
Walsh, C., Nomura, H., & van Dishoeck, E. 2015, A&A, 582, A88
Waskom, M. 2021, JOSS, 6, 3021
Wells, M., Pel, J. W., Glasse, A., et al. 2015, PASP, 127, 646
Woitke, P., Min, M., Thi, W. F., et al. 2018, A&A, 618, A57
Wright, G. S., Rieke, G. H., Glasse, A., et al. 2023, PASP, 135, 048003
Zhang, K., Pontoppidan, K. M., Salyk, C., & Blake, G. A. 2013, ApJ, 766, 82
Zhang, S., Kalscheur, M., Long, F., et al. 2023, ApJ, 952, 108
Zhu, Z., & Stone, J. M. 2018, ApJ, 857, 34
Zormpas, A., Birnstiel, T., Rosotti, G. P., & Andrews, S. M. 2022, A&A, 661, A66